Journal of Applied Research and Technology

Arellano, Ulises; Wang, Jin An; Balcázar, Luz M.; Chen, Lifang; Salmones, José; Solís, Silvia; Asomoza, Maximiliano; González, Julio
Ag/CeO2/SBA-15 hybrid catalysts for the elimination of *E. coli* in potable water system

Ag/CeO2/SBA-15 hybrid catalysts for the elimination of *E. coli* in potable water system

Ulises Arellano[b] • Jin An Wang[a]* • Luz M. Balcázar[a] • Lifang Chen[a] •
José Salmones[a] • Silvia Solís[b] • Maximiliano Asomoza[b] • Julio González[c]

[a]ESIQIE, Instituto Politécnico Nacional, 07738 Col. Zacatenco, Mexico City, Mexico
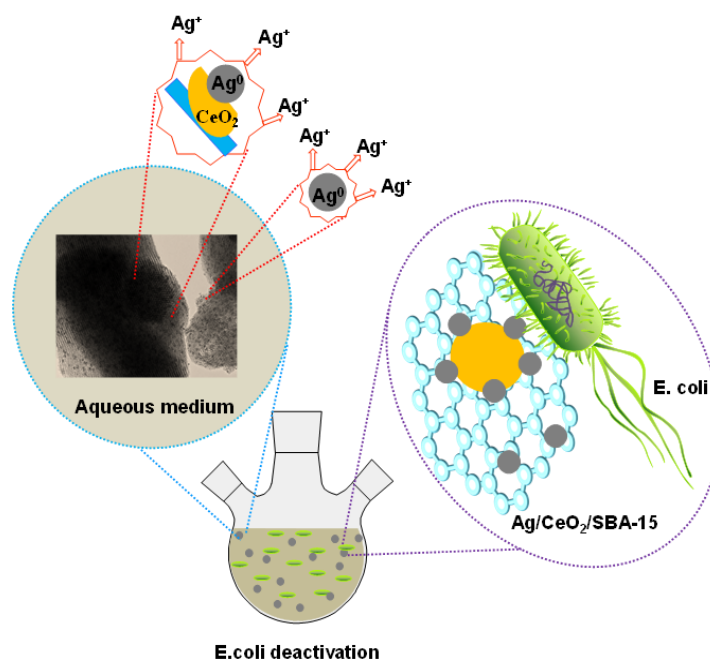[b]Departamento de Química, Universidad Autónoma Metropolitana-Iztapalapa,
Av. San Rafael Atlixco No. 186, Iztapalapa, Mexico City, Mexico
[c]Tecnologico de Estudios Superiores de Coacalco. 16 de Septiembre 54, Col. Cabecera municipal,
Coacalco de Berriozabal, Estado de México 55700, Mexico

Graphical abstract

Abstract: Hybrid Ag/CeO$_2$/SBA-15 mesoporous nanocatalysts were prepared and their bactericidal activity was evaluated aiming at elimination of *Escherichia coli (E. coli)* in the potable water system. It was found that there existed electrons transferring from Ag^0 to CeO$_2$ to form Ag$^+$/Ag^0 and Ce^{4+}/Ce^{3+} couples in the heterojunction structure, which resulted from strong interaction between Ag nanoparticles (AgNPs) and highly dispersed CeO$_2$. By increasing the Ag content from 1wt% to 3 and 5 wt% in the catalysts, the bactericidal power of Ag/CeO$_2$/SBA-15 materials significantly enhanced in the presence of both visible and UV light, which can be explained by the increasing electrons transferring function from Ag^0 to CeO$_2$ under UV-visible light irradiation. A combination mechanism of *E. coli* deactivation was proposed where *E. coli* body may be simultaneously attacked by both AgNPs and Ag$^+$ ions promoted by CeO$_2$. The former may attack the cell membrane, leading to its cleavage and disruption; and the latter may be ionized and released from AgNPs to enter inside the cell, modifying its permeability and respiration, finally resulting in complete deactivation and death.

Keywords: *E. coli*, Ag nanoparticles, hybrid catalysts, antimicrobial properties, electron transfer.

*Corresponding author.
E-mail address: jwang@ipn.mx (Jin An Wang).
Peer Review under the responsibility of Universidad Nacional Autónoma de México.

1. Introduction

E. coli is a family of bacteria in the intestine systems of humans and animals, most of which generally do not cause human health problems; however, some types of *E. coli* can result in illnesses such as diarrhea, which affects all age groups, particularly infants, travelers and adults with weakened immune systems (Mokomane, Kasvosve, Melo, Pernica, & Goldfarb, 2018). *E. coli* can survive in deteriorated foods and water systems contaminated by animals or human waste. When people consume these contaminated food or water, healthy problems such as nausea, vomiting, severe stomach pains and diarrhea may immediately take place. The worst types of *E. coli* may cause hemorrhagic diarrhea, kidney failure and even death. *E. coli* is chiefly responsible for approximately 630 million cases of diarrhea and approximately 1.3 million deaths in 2015 worldwide (Qidwai, Pandey, Kumar, Shukla, & Dikshit, 2018; Troeger et al., 2017).

Recently, nanobiotechnology has attracted increasing attention because of its cutting-edge nature and a vast spectrum of applications covering many fields, including the biomedical area. Many investigators have applied metal nanoparticles such as Ag and Au, as well as metal oxides including CuO and ZnO in the fields of medicine and environmental control (Cho, Deng, Kim. Ross, Surampalli, 2008; Huang et al., 2008; Naika et al., 2015; Padil & Cernik, 2013; Park et al., 2009; Rai et al., 2014; Shankar, Ahmad, Pasricha, & Sastry, 2003). Ag nanoparticles (AgNPs) exhibit good antibacterial activity and synergistic effects with antibiotics against a wide group of pathogenic bacteria (Spadaro, Berger, Barranco, Shapin, Becker, 1974). The antimicrobial properties of ionized Ag nanoparticles have been already known and they are widely used in tissue engineered scaffolds and devices, drug delivery systems, cancer therapy, bioanalytical diagnostics and therapeutics. It is believed that ionized Ag$^+$ joins to tissue proteins and provokes structural changes in the bacteria cellular wall and cellular membrane (Holt & Bard, 2005). Ag$^+$ has high affinity to thiol groups in cysteine residue of respiratory and transport proteins. After treatment with Ag$^+$ containing agent, DNA in microorganisms loses its replication ability and cellular proteins become distorted and

inactivated, leading to cell death (Lok et al., 2006; Schreurs & Rosenberg, 1982; Yang et al., 2009).

It is noted that when Ag^+ containing liquid agent is used for eliminating bacteria in potable water systems, it is difficult to be recovered. One possibility to avoid this disadvantage is to disperse Ag nanoparticles on a proper support. In our previous work, we supported Ag nanoparticles on a sol-gel SiO_2 solid, and found that 10wt%Ag-SiO_2 nanoparticles are very active in *E. coli* elimination for potable water treatment; moreover, the Ag-SiO_2 solid can be reused (Mendiola et al., 2017). In another work, we found that Fe–TiO_2 thin film photocatalysts present an antimicrobial efficiency in rutile phase better than in anatase phase, due to the fact that the former presents a higher contact area for the microorganism adherence and a smaller band gap energy (Eg) (Arellano, Asomoza, & Ramírez, 2011).

To our best knowledge, Ag^0 nanoparticles promoted with CeO_2 layer and dispersed on a mesoporous support SBA-15 used for *E. Coli* elimination are not yet reported and their mechanism of inhibitory action on microorganisms is not clear. Integration of nanotechnology and bacteriology may lead to possible advances in the formulation of new types of bactericides. In the present work, with the aim of obtaining highly dispersed Ag nanoparticles on solid with high bactericidal activity, a series of Ag/CeO_2/SBA-15 hybrid mesoporous catalysts with different Ag loading (1~5wt%) and 20wt% CeO_2 were synthesized. SBA-15 was selected as support because of its large surface area (500~1100 m^2/g), big pore diameter (7~10 nm) and pore volume (0.8~1.2 cm^3/g), and CeO_2 was used herein as textural and electronic promoter due to its high oxidation power and defective structure. The crystalline structure, textural properties, morphological features, and optical properties of the synthesized Ag/CeO_2/SBA-15 hybrid catalysts were characterized by X-ray diffraction (XRD), N_2 adsorption-desorption isotherms, scanning electron transmission microscopy (STEM), electron dispersive spectroscopy (EDS), UV-vis diffuse reflectance spectroscopy (DRS-UV-Vis), and X-ray photoelectron spectroscopy (XPS) techniques. Their bactericidal activity was tested in the elimination of *E. coli* under visible light and UV irradiation condition. For the first time, the promoting role of ceria on the enhancement of bactericidal activity of AgNPs resulting from the electronic functions between Ag and CeO_2 in Ag/CeO_2/SBA-15 hybrid catalysts is reported. A combination mechanism for *E. coli* elimination on the Ag/CeO_2/SBA-15 catalysts is proposed.

2. Experimental

2.1. Synthesis of SBA-15

SBA-15 was synthesized using tetraethyl orthosilicate (TEOS) as Si precursor and pluronic (P123) used as structural linker. 4g of P123 were added to 144 mL of a deionized water and 1.7 M HCl solution at 40 °C under stirring for 1 h. Subsequently, 8.6 mL of TEOS was added, drop by drop, to the above solution and was continuously stirred for 2 h. The solution was then transferred to a Teflon bottle which was tightly sealed and maintained at 100 °C for 48 h under static conditions. The white solid was filtered, washed with deionized water several times and dried at 80 °C for 4 h. The obtained samples were calcined at 550 °C in flowing air (50 ml/min) for 6 h. The temperature increasing rate was controlled at 1°C/min.

2.2. Synthesis of Ag/SBA-15, CeO₂/SBA-15 and Ag/CeO₂/SBA-15

The CeO_2 supported on SBA-15 solid was synthesized by incipient impregnation with $Ce(NO_3)_3 \cdot 6H_2O$ solution. The amount of $Ce(NO_3)_3 \cdot 6H_2O$ (Sigma-Aldrich, 99.99%) was calculated in order to obtain 20 wt% CeO_2 on SBA-15. Subsequently, the sample was washed, dried and calcined at 550 °C in air for 5 h. It was noted as CeO_2/SBA-15.

For synthesizing Ag/CeO_2/SBA-15 catalysts, the Ag was introduced by incipient impregnation in the CeO_2/SBA-15 material with an aqueous solution of $AgNO_3$ (Sigma-Aldrich, ACS reagent, 99%). The Ag content varied in order to obtain the catalyst containing 1, 3 and 5wt% Ag. Finally, the samples were dried at 70 °C and then calcined at 300 °C for 2h. These catalysts termed nAg/CeO_2/SBA-15, where n = 1, 3 and 5wt%. For comparison, a series of nAg/SBA-15 catalysts (n =1, 3 and 5wt%) were also prepared with similar method described above. Before XRD, XPS and UV-vis spectroscopic analysis the samples were reduced with hydrogen.

2.3. Catalysts characterization

All the materials were characterized by X-ray diffraction (XRD) using a Siemens D500 diffractometer. The wide angle X-ray scattering patterns were obtained in the 2θ intervals of 20 to 80 °, with a step of 0.02 ° and a measuring time of 2.67 seconds in each point.

The N_2 adsorption-desorption isotherms were measured in a Micromeritics ASAP2000 instrument, using the Brunauer-Emmett-Teller (BET) method for the surface area calculation and the Barrett-Joyner-Halenda method (BJH) model for calculation of distribution of pore size. Before N_2 adsorption, the samples were thermally degassed under vacuum at 200 °C for 24 h.

The TEM micrographs were obtained with a high resolution microscope (HRTEM Jeol 2100F), using as a light source a field emitter and 200 kV of accelerator. It has a resolution of 1.86 Å. In the selected area of the TEM micrograph, element analysis was determined using electron dispersive spectroscopic (EDS) technique.

The UV-vis spectra were obtained by an Evolution-220 spectrometer (Thermo Fisher scientific) at room temperature.

The chemical valences and oxidation states of O, Si, Ag and Ce in the surface of Ag/CeO_2/SBA-15 nanomaterials were

analyzed by X-ray photoelectron spectroscopy (XPS) technique (Escalab 2500 Termo VG Scientific), coupled with an Ar ion cannon, and equipped with a microscope that projects the image on a screen to observe the analysis position.

2.4. Preparation of E. coli growth medium

Saline solution: 500 mL of 0.9% NaCl saline solution was prepared, from which 9 mL solution was distributed in threaded tubes, and then sterilized in an autoclave at 121 °C and 15 lb/in² of pressure for 15 min.

LB (Luria Bertani) growth medium: 10 g/L of casein peptone, 10 g/L sodium chlorine and 5 g/L yeast extract suspended in 800 mL of distilled water. It was stirred and filled up to 1 L. The pH was adjusted at 7.2 ± 0.2 with 10 N sodium hydroxide solution and sterilized in an autoclave at 121 °C and 15 lb/in² of pressure lasting for 15 min.

EMB (eosine methylene blue) agar: 36 g of EMB medium were suspended in 1 L of distilled water and left to sit for 5 min to later be heated up to boiling point for 1 ~ 2 min until dissolution. The EMB medium was adjusted at pH 7.2 ± 0.2 with sodium 10 N hydroxide solution and was treated under the same experimental conditions employed for the previous LB growth medium.

Preparation of petri dishes: The EMB medium was left to cool until 50 °C and distributed it into petri dishes in a sterile area. They were solidified to later be incubated in a period of 24 h.

2.5. Determination of bacteria number

The number of bacteria present in a given volume was determined using the cell plaque count technique and by the determination of turbidity. The first technique allows quantifying the number of viable bacteria (colony forming units CFU), and the second measures the total biomass of the microbial population.

The steps of plaque-count technique are described as follows: (1) An aliquot of 1 mL was taken in sterile condition from the medium where the deactivation reaction was carried out. (2) It was diluted in a threaded tube with 9 mL saline solution, this being a dilution of 10^{-1} and then stirred. (3) An aliquot of 1 mL was taken from the first tube (10^{-1} dilution) and was taken to a new tube with 9 mL of saline solution, this being the dilution 10^{-2}. (4) The steps 2 and 3 were repeated until a dilution of 10^{-10} was reached. (5) 0.05 mL of each one of the dilutions was taken, and grown in petri dishes previously prepared with solid EMB medium. (6) The inoculum was dispersed over the entire surface of the agar with the help of a sterile glass handle. (7) It was incubated at 37 °C. (8) The counts of the colony forming units (CFU/min) were carried out for 24, 48 and 72 h. The dilutions were prepared by duplication.

2.6. Measurement of E. coli growth kinetics

Before carrying out the bacteria deactivation experiment, the life cycle of the *E. coli* population was measured. This was carried out by measuring the turbidity according to the following procedure: two threaded tubes were prepared at the same time used as the reactor where the deactivation was carried out with 4.5 and 135 mL of LB medium, respectively. Afterwards, in a sterile area, they were inoculated with 0.5 mL and 10 mL of *E. coli* at 37 °C. The growth was monitored by spectrophotometer during 6 h in the threaded tubes in the following manner: (1) the spectrophotometer was calibrated at 580 nm; (2) the previously inoculated tubes were stirred with the help of a vortex; (3) The absorbance was measured at intervals of 1 h; (4) the measurements were carried out as the stationary phase was reached.

2.7. Measurement of E. coli deactivation kinetics

A 250 mL Pyrex beaker glass was used as a reactor which was placed over a magnetic stirrer. The *E. coli* deactivation reaction was performed at atmospheric pressure at 37 °C with stirring. The reaction was maintained for 1 h and monitored by taking aliquots of 1 mL every 30 min. The material mass used was 100 mg for every 100 mL of LB medium previously inoculated with *E. coli*. Once it reached the stationary phase of growth, a sample of 1 mL was taken in sterile reactor conditions and labeled as Zero Time. Afterwards, the material was placed in the reactor to commence the deactivation. Samples were taken at 30 and 60 min and the plaque technique was applied for analysis, and they were then labeled as Time 1 and 2, respectively. The experiments were performed by duplication and each point in Figs. 8-10 represented the average of the measurements.

3. Results and discussion

3.1. Crystalline structure of the catalysts – XRD analysis

Figure 1 shows the X-ray diffraction patterns of the Ag/SBA-15, CeO_2/SBA-15, and Ag/20wt%CeO_2/SBA-15 catalysts. For the Ag/SBA-15 samples, Figure 1, the peaks at 2θ = 39.0, 44.6, 64.8 and 78.1° correspond to the reflections of (111), (200), (220) and (311) planes of Ag^0 nanocrystals (JPCDS No. 89-3722). The wide peak between 20 and 35° is characteristic of the ordered mesoporous silica, herein, SBA-15 support. The intensity of the peaks slightly increases on increasing of Ag content, indicating the slight growth of the crystallite size.

For the 20wt%CeO_2/SBA-15 sample, Figure 2, the powder diffractogram signals with 2θ at 28.7, 33.9, 47.6, 56.8, 65.0, and 70.1° correspond to the reflections of the (111), (200), (220), (311), (222), and (400) planes of CeO_2 phase with cubic structure

(JCPDS No. 81-0792). For the Ag/CeO$_2$/SBA-15 samples, both CeO$_2$ and Ag phase are present. Silver crystallite size slightly gains on increasing of Ag content. As the typical diffraction peak at around 33° of 2θ that corresponds to Ag$_2$O crystals is absent, Ag$_2$O does not exist in all the samples (Wang et al., 2012). After calcination, sliver remained as metallic nanoparticles not as Ag$_2$O which is common as reported by many other investigators (Sandoval, Aguilar, Louis, Traverse, & Zanella, 2011; Wang, Aguilar-Rıos, & Wang, 1999).

3.2. Textural properties – N$_2$ physisorption isotherms
Figure 3 shows the loops of N$_2$ adsorption-desorption isotherms of the different catalysts. The shape of all the loops indicates type IV with H1 hysteresis that is a typical character of cylinder type mesoporous solids, according to the classification of the International Union of Pure & Applied Chemistry (IUPAC) (Sing, 1985). The hysteresis cycle of the 1Ag/20CeO$_2$/SBA-15 almost coincides with the one CeO$_2$/SBA-15 solid, indicating that a small amount of Ag nanoparticles introducing onto the surface of CeO$_2$/SBA-15 does not modify the pore structure system. The other two materials with 3 and 5wt% Ag content show a downward turn relative to CeO$_2$/SBA-15, resulting from a slight decrease in volume of mesopores. All materials have a monomodal pore size distribution between 3.5 and 8.5 nm with a maximum 6 ~7 nm, Figure 4. The textural parameters including the surface area, average pore size and pore volume calculated from the N$_2$ desorption isotherms are reported in Table 1.
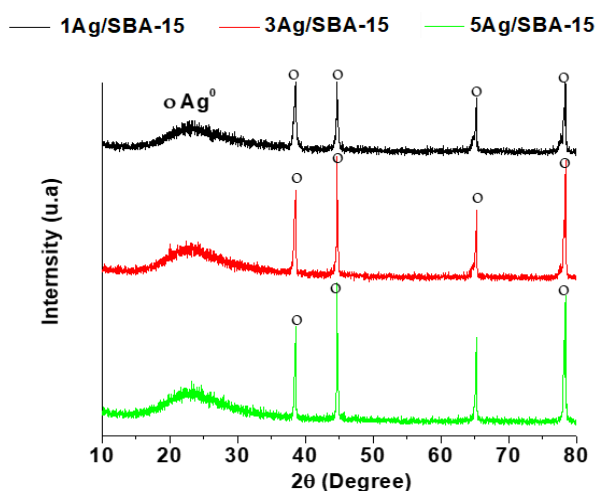

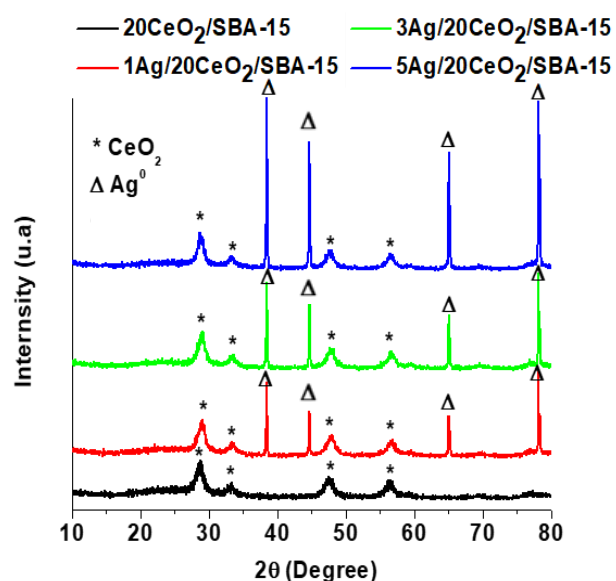Figure 1. XRD patterns of Ag/SBA-15 catalysts.

Figure 2. XRD patterns of CeO$_2$/SBA-15 and Ag/CeO$_2$/SBA-15 catalysts.
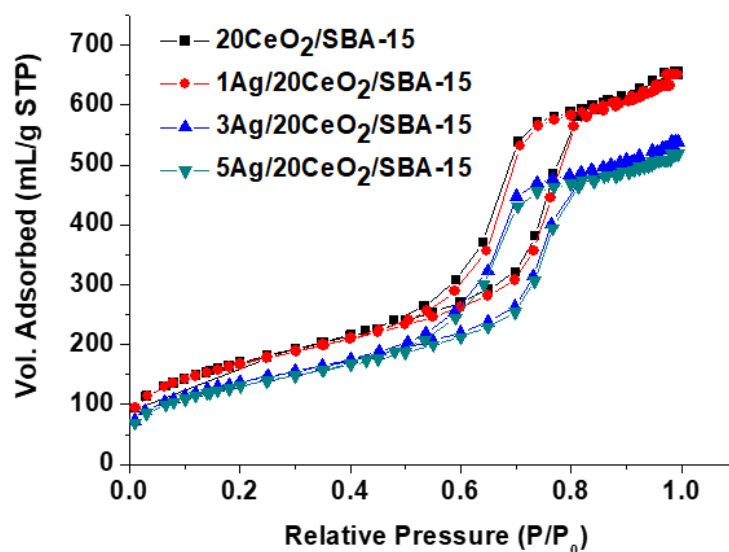
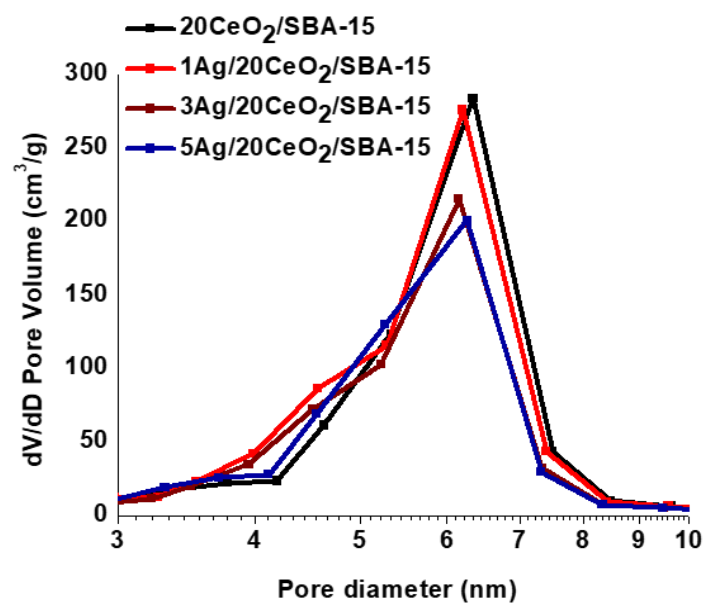Figure 3. Loops of N_2 adsorption-desorption isotherms of CeO_2/SBA-15 and Ag/CeO_2/SBA-15 catalysts.

Figure 4. Pore size distribution of CeO_2/SBA-15 and Ag/CeO_2/SBA-15 catalysts.

Table 1. Textural properties of the CeO_2/SBA-15 and Ag/CeO_2/SBA-15 samples.

Sample	S_A (m^2/g)	D_p (nm)	V_p (cm^3/g)
$20CeO_2$/SBA-15	616.4	6.7	1.026
$1Ag/20CeO_2$/SBA-15	604.1	6.6	1.001
$3Ag/20CeO_2$/SBA-15	499.6	6.7	0.836
$5Ag/20CeO_2$/SBA-15	478.1	6.8	0.811

S_A: surface area (BET); V_p: pore volume; D_p: average pore diameter.

When CeO_2 was loaded on the SBA-15 support, the surface area diminished from 1042.5 m^2/g for pure SBA-15 to 616.4 m^2/g for CeO_2/SBA-15. For the Ag/CeO_2/SBA-15 materials, both the surface area and pore volume values slightly decreased on increasing of Ag loading. Because the average pore diameter remained 6.6~6.8 nm and the Ag nanoparticles have average size around 12 nm as confirmed by TEM observation, therefore, most Ag nanoparticles are deposited on the outside of pores and higher content of Ag nanoparticles leads to possible blocking of some mesopores that may diminishes the pore volume and surface area.

3.3. Morphological features – TEM observations and EDS analysis

Figure 5 shows the TEM micrographs of SBA-15 and Ag/CeO_2/SBA-15 materials. For SBA-15 support, Figure 5A, well-ordered pore structure and hexagonal morphological feature was observed when the electron beam was parallel to the main axis. The average pore diameter of the SBA-15 support is approximately 7 nm, in agreement with N_2 adsorption-desorption measurement data. For the CeO_2/SBA-15 solid, Figure 5B, the small patches belong to CeO_2 phase and they are homogeneously dispersed on surface of the SBA-15. Close observations by TEM technique confirm that most of Ag particles have size between 5 and 15 nm on the surface of catalysts. Some CeO_2 are formed as small patches on the surface of SBA-15 on which some Ag particles are anchored or dispersed (Figure 5C) as confirmed by the corresponding EDS analysis (Figure 5D). Ag particles strongly interact with CeO_2 patches, forming Ag-CeO_2 heterojunction structure in the interfaces due to the strong interaction between them.

It is noteworthy that because CeO_2 are coated on the surface of SBA-15 support before Ag impregnation, and CeO_2 are well coated on the surface of SBA-15 as confirmed by TEM,

therefore, Ag nanoparticles should be principally dispersed on the CeO_2 layer but not in the SBA-15 support. However, we cannot rule out the possibility of a small amount of Ag nanoparticles are dispersed on SBA-15 support as some area of SBA-15 is free of CeO_2 loading.

3.4. Photoproperties UV-vis diffuse reflectance spectroscopy (DRS-UV-Vis)

Figures 6 and 7 show the DRS-UV-Vis spectra and plots of Kubelka-Munk function $(\alpha h\nu)^{1/2}$ versus energy $(h\nu)$ of the CeO_2/SBA-15 and Ag/CeO_2/SBA-15. The UV absorption band at around 320 nm is assigned to the $O^{2-} \rightarrow Ce^{4+}$ charge transfer in the CeO_2 particles (Khan et al., 2014). The band at 520 nm resulted from absorption of Ag^0 plasmon nanoparticles (Van Dao et al., 2018). For Ag^0 plasmon band, there is a significant red-shift to around 500 nm in comparison with Ag/CeO_2 where it locates approximately 400 nm, which is similar to the results (430~450 nm) reported by other authors (Khan et al., 2014; Van Dao et al., 2018), strongly indicating that electrons in Ag may transfer to CeO_2 due to the strong interaction between them in our Ag/CeO_2/SBA-15 hybrid catalysts via localized surface plasmon resonance mechanism (Warule et al., 2002). Ag dispersing on pure CeO_2 may generate weak electron transfer because of the relatively weak interaction between Ag particles and ceria with large particles. When Ag was loaded on dispersed CeO_2 layer on SBA-15 support, not only the Ag dispersion was significantly improved as the surface area of CeO_2/SBA-15 (616 m^2/g) is approximately 6~8 times greater than that of pure ceria (around 50-80 m^2/g), but the amount of ceria used was significantly reduced also. Moreover, in the Ag/CeO_2/SBA-15, heterojunction structure in the interfaces was formed as evidenced in Figure 5C; all these favor the charge transfer between Ag and CeO_2.
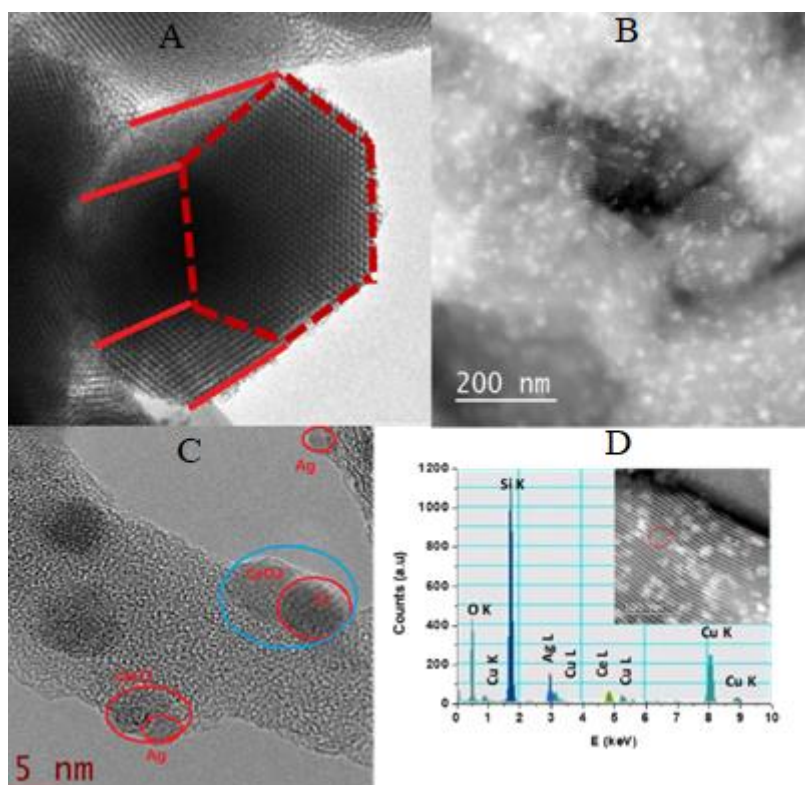
Figure 5. TEM micrographs of 3Ag/20CeO$_2$/SBA-15 and EDS profile of the selected area.
(A) SBA-15. (B) 20wt%CeO$_2$/SBA-15. (C) 5Ag/20CeO$_2$/SBA-15;. (D) EDS of 5Ag/20CeO$_2$/SBA-15.
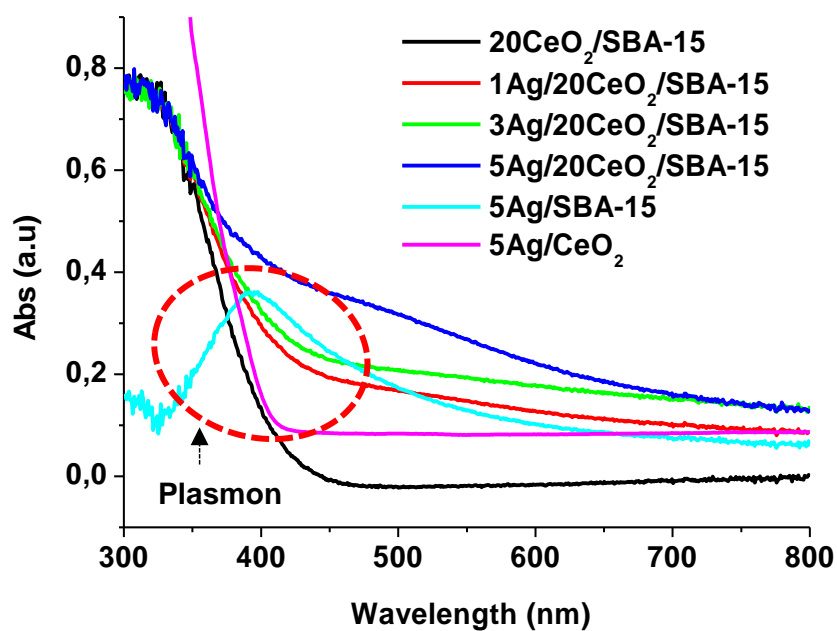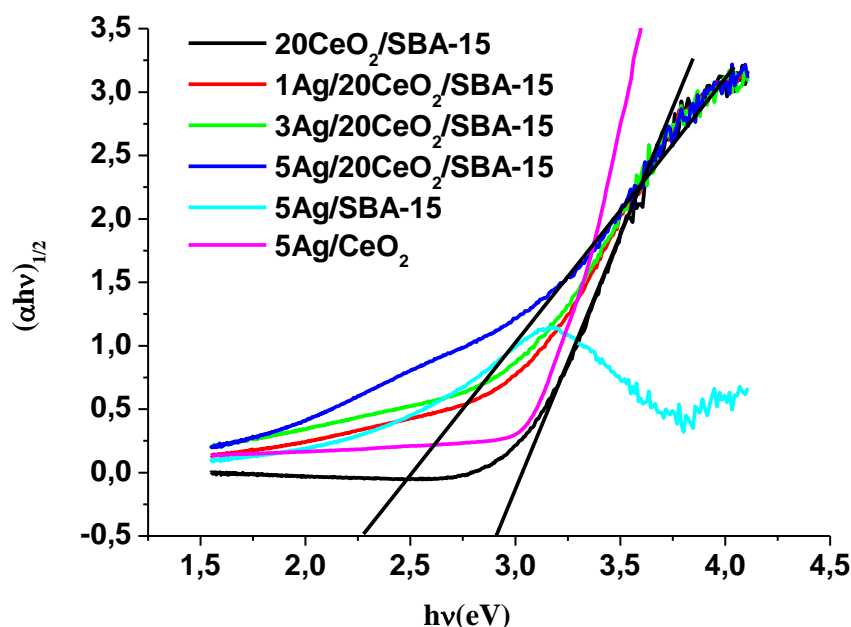

Figure 6. DRS-UV-Vis spectra of different catalysts.

Figure 7. Kubelka-Munk function $(\alpha h\nu)^{1/2}$ versus energy $(h\nu)$ plots.

The values of band gap energy (E_g) were calculated by the Kubelka-Munk method, which consists of plotting the product $h\nu$ (the energy of light) on the abscissa, and the $(\alpha h\nu)^{1/2}$ on the ordinate, where α is the coefficient of absorption of the material. E_g values of the different catalysts are reported in Table 2. It decreased from 2.8 eV for CeO$_2$/SBA-15 to 2.6, 2.5 and 2.2 eV for the Ag/CeO$_2$/SBA-15 samples with Ag loading varying from 1 to 3 and 5wt%, respectively. It is noted that Eg value for the sample 5Ag/CeO$_2$ is around 3.0 eV, which is the highest value amongst six samples. The Eg values of all the Ag/CeO$_2$/SBA-15 samples fall in the near visible light region, indicating that the Ag/CeO$_2$/SBA-15 catalysts possess capacity of absorbing visible light; and therefore, they may be activated in the presence of visible light. The red-shift of the absorption band and the decrease of E_g value on increasing of Ag content indicate the electron transfer and strong interaction between AgNPs and highly dispersed CeO$_2$ in the Ag/CeO$_2$/SBA-15 catalysts. We did not found the obvious electron transfer between Ag and SBA-15 according to UV-visible characterization (Figs. 6 and 7). Electron transfer from Ag^0 to Ce^{4+} in the Ag/CeO$_2$ seems not obvious as its E_g (3.0 eV) value remained similar to the Eg value of pure CeO$_2$, which probably results from the relatively weak interaction between AgNPs and CeO$_2$.

3.5. Surface chemical valences and metal oxidation state – XPS analysis

Figure 8 shows the XPS spectra and their deconvolution of the Ag/CeO$_2$/SBA-15 materials. Figure 8B shows the core level of Si 2p3/2 in the region between 101 and 106 eV, confirming Si^{4+} in the crystalline structure of SBA-15. Figure 8B shows the O1s spectra of the Ag/CeO$_2$/SBA-15 materials. It can be deconvoluted into two parts with peak maxima at 533.5 and 532.8 eV, which are assigned to oxygen in surface OH species and lattice O^{2-} in CeO$_2$ or SBA-15, respectively (Pereira, Blouin, Pillonnet, & Guay, 2014). The latter was not further deconvoluted and separated.

Figure 8C shows the Ag 3d core levels of XPS spectra in the region between 364 eV and 380 eV. These Ag 3d peaks consist of two components, one is indicated by two peaks at 374.9 and 368.2 eV which are assigned to Ag^0 3d3/2 and Ag^0 3d5/2, respectively. The other two small peaks at 373.1 eV and 367.6 eV are assigned to Ag$^+$ 3d 3/2 and Ag$^+$ 3d5/2, respectively (Kaspar, Droubay, Chambers, & Bagus, 2010). The peak widening may result from a strong interaction between the Ag^0 nanoparticles and CeO$_2$. The coexistence of both Ag^0 and Ag$^+$ indicates electrons transferring from Ag^0 to CeO$_2$ resulting from strong interaction between them. Electron transferring from Ag^0 to CeO$_2$ leads to Ag partially oxidation, generating Ag$^+$

species, which is in good agreement with the results obtained by DRS-UV-Vis characterization.

Figure 8D shows the core levels of XPS spectra of Ce in the catalysts, which are relatively complicated due to the multicomponents. The Ce3d spectrum is composed of multiple doublets (u and v) corresponding to spin-orbit split of 3d3/2 and 3d5/2. By fitting with Gaussian function, the Ce3d spectrum contains both Ce^{3+} and Ce^{4+} oxidation states. The components labeled as v_o, v', u_o and u' indicate the presence of Ce^{3+} oxidation states and the peaks labeled as v, v'', v''', u, u'' and u''' reveal the presence of Ce^{4+} oxidation states (Maslakov et al., 2018; Vargas et al., 2018). The peaks u_0 and v_0 are well defined, indicating that all the hybrid materials contain a certain amount of Ce^{3+} ions which confirms the presence of nonstoichiometric ceria incorporated into their defective lattice structure. These hybrid materials have a mixture of Ce^{3+}/Ce^{4+} species on their surface and crystalline structure, where the Ce^{4+} species are the predominant component. The formation of Ce^{3+} ions also indicates electrons transferring from Ag^0 to CeO_2. When some Ce^{4+} accepts an electron from Ag^0, its oxidation state was reduced to Ce^{3+}. The formation of Ce^{3+} ions may also result from the existence of oxygen defects in the crystalline structure of CeO_2, for remaining the local charge balance.

Table 2. Band gap energy (Eg) of different samples.

| Samples	Eg (eV)
$20CeO_2$/SBA-15	2.8
$1Ag/20CeO_2$/SBA-15	2.6
$3Ag/20CeO_2$/SBA-15	2.5
$5Ag/20CeO_2$/SBA-15	2.2
$5Ag$/SBA-15	----
$5Ag/CeO_2$	3.0

3.6. Antibacterial activity evaluation

Figure 9 shows the number of viable CFU/mL of *E. coli* with respect to the exposure time on catalysts in a black box. In the absence of light but with CeO_2/SBA-15, *E. coli* remains viable with a population of 2.50×10^8 CFU/mL during the 60 min deactivation, confirming that CeO_2/SBA-15 does not present any bactericidal power. For 5Ag/SBA-15 solid, it exhibited

a certain bactericidal power, which is quite similar to the Ag/CeO_2/SBA-15 materials. However, the activity of Ag/SBA-15 or Ag/CeO_2/SBA-15 catalysts is very low in the absence of light.

In the presence of visible light, the variations of the number of viable CFU/mL of *E. coli* as function of time are shown in Figure 10. Without catalyst, the number of viable CFU/mL of *E. coli* remained unchanged under 60 min of visible light. However, the number of viable CFU/mL of *E. coli* significantly diminished when catalysts were added. The activity enhanced as Ag nanoparticles were present on CeO_2/SBA-15. Higher Ag loading favored the improvement of the bactericidal activity. In comparison with the results shown in Fig. 9, results obtained in the visible light indicated that visible light may activate all Ag containing catalysts. However, the bactericidal activity of the catalysts needs further improvement as part of *E. coli* still remained alive under such condition.

In the presence of UV light, Figure 11, when Ag/CeO_2/SBA-15 catalysts were used, the viable population of *E. coli* rapidly diminished after 30 min of UV light irradiation, depending on the Ag content in the catalyst. At 60 min, approximately 3% and 2.5% of *E. coli* survived in the presence of $1Ag/CeO_2$/SBA-15, and $3Ag/CeO_2$/SBA-15 catalysts, and no any *E. coli* survived with $5Ag/CeO_2$/SBA-15 catalyst. By increasing the Ag content in the catalysts, the bactericidal power of Ag/CeO_2/SBA-15 materials greatly enhanced. The $5Ag/20CeO_2$/SBA-15 catalyst exhibits the best bactericidal activity. Unexpectedly, the bactericidal activity of Ag/SBA-15 was not significantly promoted in the UV light irradiation with respect to that shown in the visible light. This result may indicate that the interaction between AgNPs and SBA-15 is not significant and the electron transfers between Ag and SBA-15 did not occur, which clearly differs from that took place in the Ag/CeO_2/SBA-15 catalysts.

Figure 12 presents the viable colonies of *E. coli* in EMB medium before and after the deactivation with the $5Ag/20CeO_2$/SBA-15 sample in the presence of UV light. In Figure 12A, at time zero the greatest number of viable colonies of *E. coli* was observed. After 30 minutes of exposition to UV light, the *E. coli* colonies presented the characteristic metallic green color. Inhibition of the colonies of *E. coli* was clearly observed (Figure 12 B), and the total deactivation was realized after 60 min (Figure 12C).
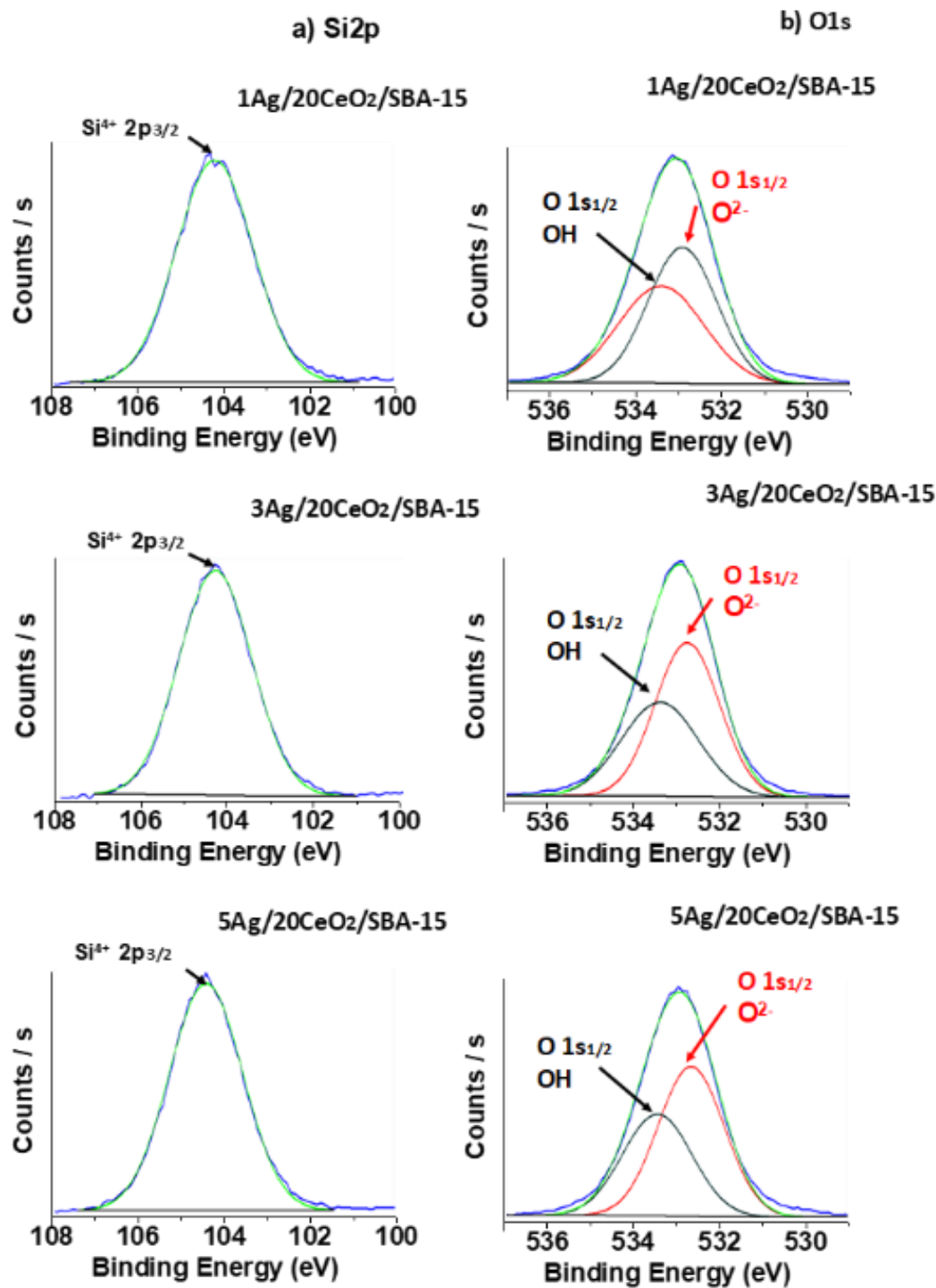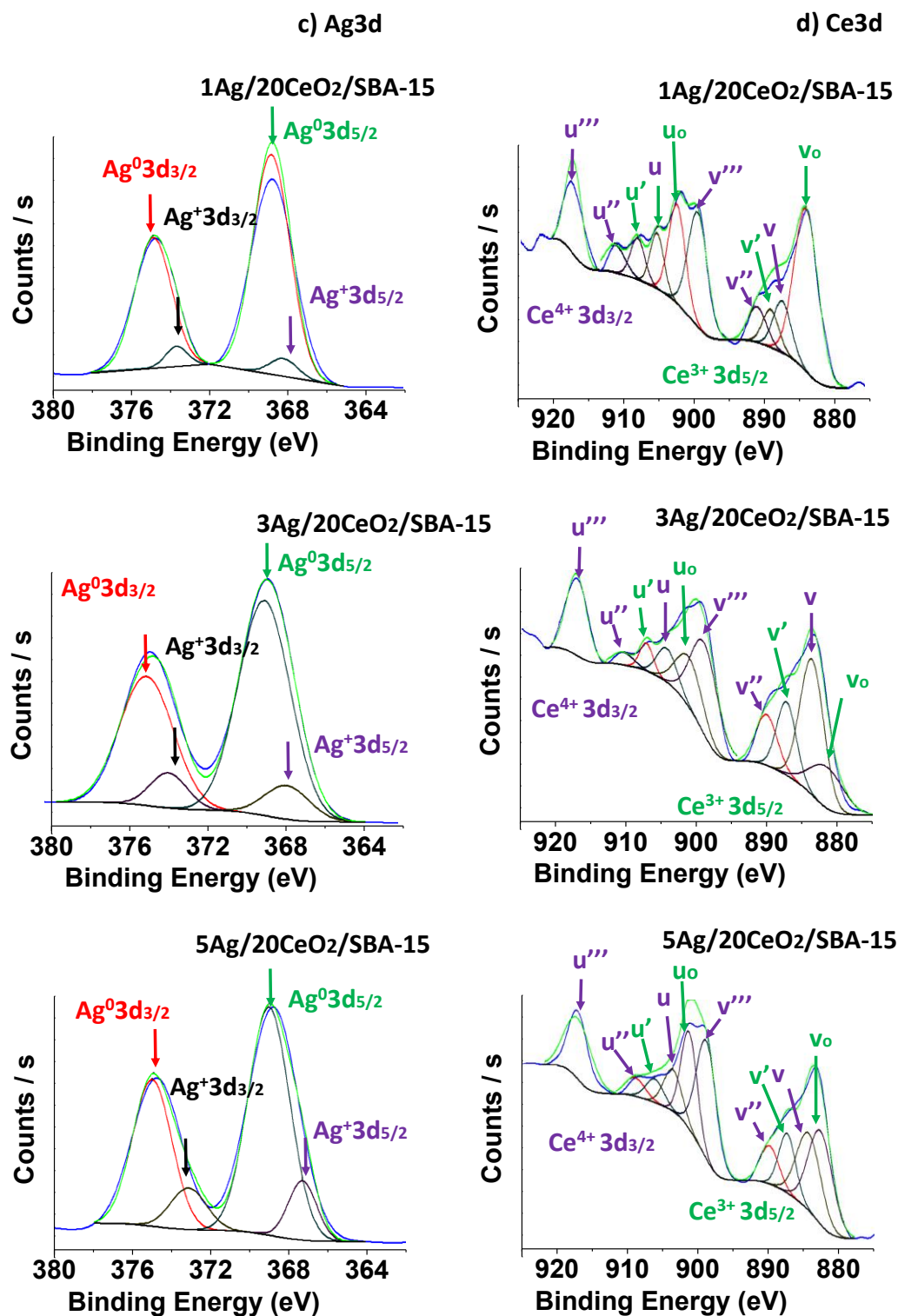
(A) Si2p. (B) O1S. (C) Ag3d. (D) Ce3d.

Figure 8. Deconvolution of the XPS spectra of Ag/20Ce/SBA-15.
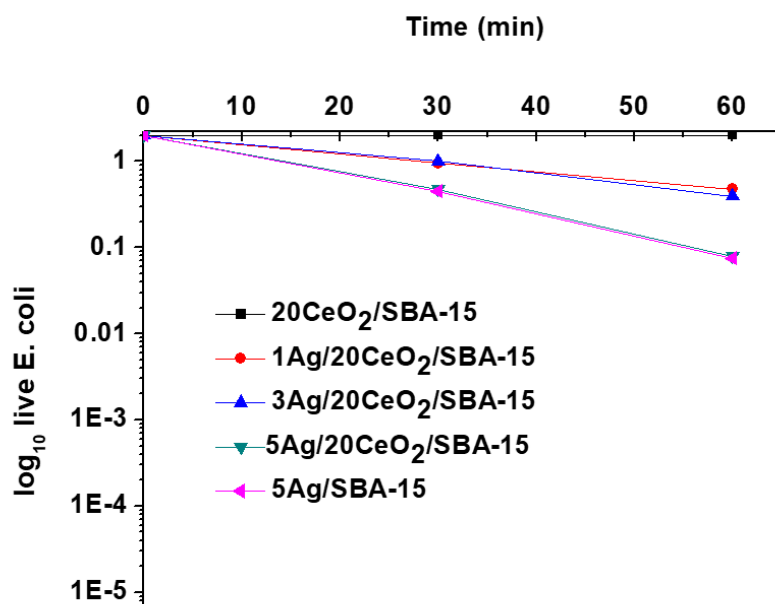
Figure 9. *E. coli* deactivation in the absence of light with catalysts.
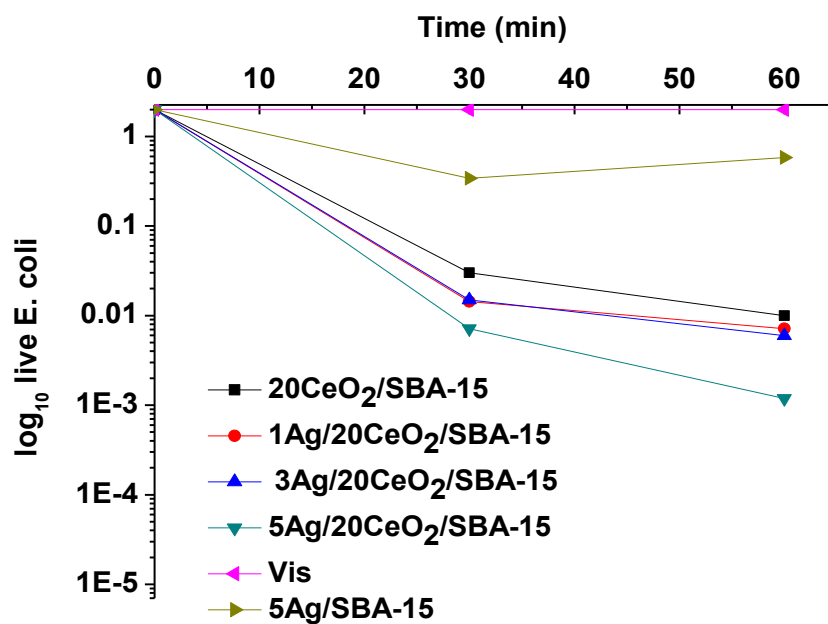

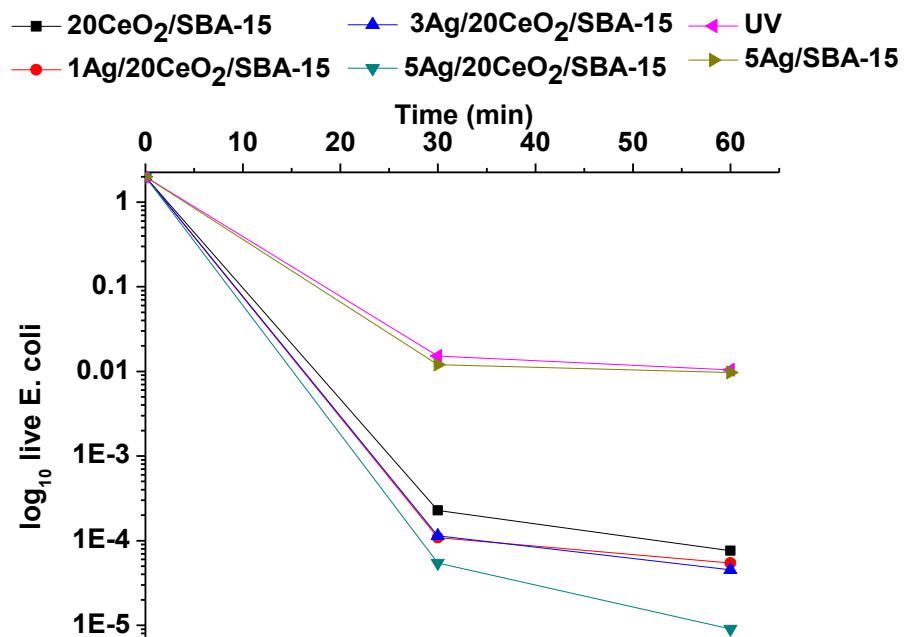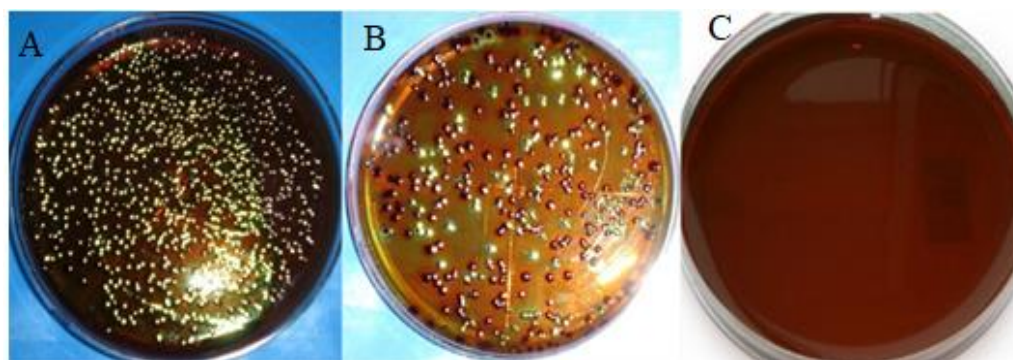Figure 10. *E. coli* deactivation in the present of visible light with catalysts.

Figure 11. *E. coli* deactivation in the present of UV light with catalysts.

(A) *E. coli* at time zero. (B) *E. coli* at time 30 min. (C) *E. coli* at time 60 min.

Figure 12. Bacteria viables of *E. coli* in EMB media.

3.7. Discussion of the E. coli deactivation mechanism

In this work, the increment of bactericidal power of the Ag/CeO$_2$/SBA-15 with respect to 5Ag/SBA-15 or CeO$_2$/SBA-15 is partially attributed to the formation of a heterojuction structure between Ag and CeO$_2$ particles (Figure 5C), resulting from a strong interaction between them. XPS analysis confirmed that electrons in Ag nanoparticles may transfer to CeO$_2$, resulting in Ce^{4+} being partially reduced into Ce^{3+}; and in turn, Ag^0 being partially oxidized to Ag$^+$ species. Therefore, there exist both Ag/Ag$^+$ and Ce^{3+}/Ce^{4+} couples in the surface of the Ag/Ce/SBA-15 catalysts. In the reaction media Ag$^+$ species may be released from the surface of Ag/CeO$_2$/SBA-15 catalysts and they can attack the cell membrane and/or phagocytosis of the adsorbed *E. coli* where Ag$^+$ most probably binds to electron donor groups such as thio, amino, imidazole carboxylate and phosphate containing sulfur, oxygen, and nitrogen, leading to the deactivation of *E. coli* (Kawashita et al. 2000; Lok et al., 2006; Yang et al., 2009).

E. coli body has a length of approximately 2 μm with a diameter around 0.5 μm; it is much greater than the AgNPs and crystallite size of our catalysts. Therefore, *E. coli* can stick to several active particles of catalyst, and its body may be simultaneously attacked by several AgNPs or Ag$^+$ species, accelerating the rate of its deactivation and death. Moreover, CeO$_2$ possesses a certain oxidation power and may directly participate in the *E. coli* deactivation under UV irradiation (Figs. 10 and 11). As a result, for the hybrid Ag/CeO$_2$/SBA-15 catalyst, AgNPs, Ag$^+$, and CeO$_2$ may simultaneously contribute to the elimination of *E. coli*, where Ag NPs and Ag$^+$ take the predominating role and CeO$_2$ chiefly plays the role as electronic promoter. On the basis of the previous work (Castellano et al., 2007; Hwang et al., 2008; Sondi & Salopek-Sondi, 2004) and the results obtained from this work, a possible combination mechanism of *E. coli* deactivation catalyzed with Ag/CeO$_2$/SBA-15 materials is proposed and demonstrated in Figure 13.
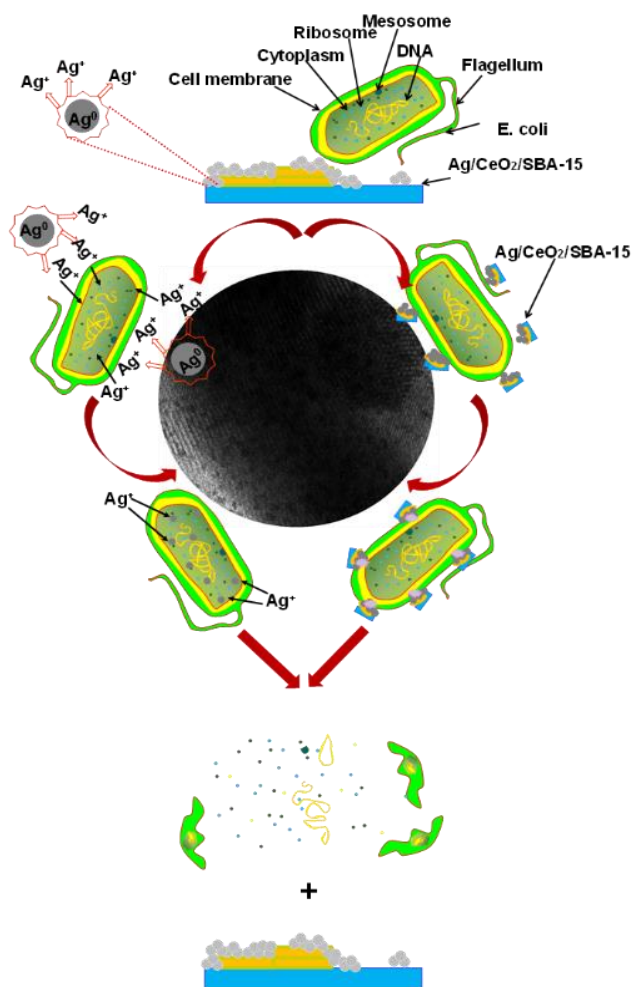

Figure 13. *E. coli* deactivation mechanism on the Ag/Ce/SBA-15 catalysts.

The *E. coli* deactivation mechanism involves several steps: (1) adherence of *E. coli* on the surface of the Ag/CeO$_2$/ SBA-15 by adsorption or electrostatic attraction; (2) AgNPs, Ag$^+$ species and CeO$_2$ particles simultaneously attack the cell membrane of *E. coli* on the attaching points; (3) cleavage of the cell membrane resulting from decomposition of the organic compounds that make up *E. coli*; (4) deactivation or death of the *E. coli* body by modification permeability and respiration.

In the second step, on one hand, some Ag$^+$ species released from Ag/CeO$_2$/SBA-15 materials under the reaction media may penetrate the cell wall to enter inside of the *E. coli* body and thus destroy the sulfur and phosphorus containing compounds such as proteins and DNA that may inhibit DNA replication, resulting in loss of cell viability and ultimately cell death (Castellano et al., 2007; Hwang et al., 2008; Sondi & Salopek-Sondi, 2004). On the other hand, the large particles of Ag/CeO$_2$/SBA-15 may not enter the body, but they may disrupt or destroy the outer cell membrane by generating pores or holes on it. As a consequence, the cell membrane potential decreases and the oxidative stress increases within the *E. coli* body. These actions decouple the respiratory chain of the *E. coli* and finally lead to its death.

It is also reported that the presence of free radicals from AgNPs may participate in the elimination of *E. coli* (Yang et al., 2009). In our catalysts, surface OH species on AgNPs and CeO$_2$ may transfer electrons to OH$^{\cdot}$ free radicals under irradiation of visible and UV lights. When photoenergy is absorbed from a light source, holes in valence band and electrons in Ce 3d orbital conductive band can be generated. Electrons are transferred from the O 2p valence band to the Ce 3d orbital in the CeO$_2$ crystals. When electrons are trapped by hydroxyl, active oxygen species such as HO$^{\cdot}$ and superoxide ($\cdot$O$_2$) radicals can be generated, which are highly reactive oxidants and can attack the *E. coli* adsorbed on the particle surface (Wang et al., 2014). Therefore, *E. coli* deactivation may be also interrelated to the formation of free radicals from the surface of AgNPs and CeO$_2$ because free radicals may result in the cell membrane damage.

4. Conclusions

In the hybrid Ag/CeO$_2$/SBA-15 catalysts, a phenomenon of electrons transferring from AgNPs to CeO$_2$ was confirmed by XPS analysis and UV-vis characterization, which results in generation of Ag^0/Ag$^+$ and Ce^{3+}/Ce^{4+} couples in the surface of Ag/CeO$_2$/SBA-15 catalysts. For *E. coli* deactivation, Ag/CeO$_2$/SBA-15 solids were active in the presence of both visible light and UV light. Its bactericidal activity was significantly enhanced in comparison with CeO$_2$/SBA-15 and Ag/SBA-15, depending of Ag content. Electrons transferring from Ag to CeO$_2$ favored the enhancement of oxidation power and bactericidal capacity of these hybrid catalysts. It is proposed that *E. coli* body can be simultaneously attacked by several AgNPs, Ag$^+$ ions or CeO$_2$ *via* a combination mechanism, destroying its outer cell membrane or entering inside its body to interact with the protein compounds that control the cell viability, leading to complete deactivation and death. These hybrid Ag/CeO$_2$/SBA-15 nanomaterials with high bactericidal activity are especially promising for *E. Coli* elimination when taking into account the resistance to the environment and antibiotics of variety of bacterial strains.

Acknowledgments

References

Arellano, U., Asomoza, M., & Ramírez, F. (2011). Antimicrobial activity of Fe–TiO2 thin film photocatalysts. *Journal of Photochemistry and Photobiology A: Chemistry, 222*, 159-165. https://doi.org/10.1016/j.jphotochem.2011.05.016

Castellano, J. J., Shafii, S. M., Ko, F., Donate, G., Wright, T. E., Mannari, R. J., ... & Robson, M. C. (2007). Comparative evaluation of silver-containing antimicrobial dressings and drugs. *International Wound Journal, 4*(2), 114-122. https://doi.org/10.1111/j.1742-481X.2007.00316.x

Choi, O., Deng, K., Kim. N., Ross, L., Surampalli, R., & Hu, Z. (2008). The inhibitory effects of silver nanoparticles, silver ions, and silver chloride colloids on microbial growth. *Water Research, 2*, 3066-3074. https://doi.org/10.1016/j.watres.2008.02.021

Vargas, O. G., De los Reyes Heredia, J. A., Suárez-Toriello, V. A., Rangel, R. H., Wang, J. A., & Chen, L. F. (2018). Characterization of structural and optical properties of the mesoporous Ce-MCM-41 hybrid materials. *Journal of Materials Science: Materials in Electronics, 29*(18), 15621-15631. https://doi.org/10.1007/s10854-018-9154-5

Holt, K. B., & Bard, A. J. (2005). Interaction of silver (I) ions with the respiratory chain of Escherichia *coli*: an electrochemical and scanning electrochemical microscopy study of the antimicrobial mechanism of micromolar *Ag. Biochemistry, 44*(39), 13214-13223. https://doi.org/10.1021/bi0508542

Huang, Z., Zheng, X., Yan, D., Yin, G., Liao, X., Kang, Y., ... & Hao, B. (2008). Toxicological effect of ZnO nanoparticles based on bacteria. *Langmuir, 24*(8), 4140-4144. https://doi.org/10.1021/la7035949

Hwang, E. T., Lee, J. H., Chae, Y. J., Kim, Y. S., Kim, B. C., Sang, B. I., & Gu, M. B. (2008). Analysis of the toxic mode of action of silver nanoparticles using stress-specific bioluminescent bacteria. *Small, 4*(6), 746-750. https://doi.org/10.1002/smll.200700954

Kaspar, T. C., Droubay, T., Chambers, S. A., & Bagus, P. S. (2010). Spectroscopic evidence for Ag (III) in highly oxidized silver films by X-ray photoelectron spectroscopy. *The Journal of Physical Chemistry C, 114*(49), 21562-21571. https://doi.org/10.1021/jp107914e

Kawashita, M., Tsuneyama, S., Miyaji, F., Kokubo, T., Kozuka, H., & Yamamoto, K. (2000). Antibacterial silver-containing silica glass prepared by sol–gel method. *Biomaterials, 21*(4), 393-398. https://doi.org/10.1016/S0142-9612(99)00201-X

Lok, C. N., Ho, C. M., Chen, R., He, Q. Y., Yu, W. Y., Sun, H., ... & Che, C. M. (2006). Proteomic analysis of the mode of antibacterial action of silver nanoparticles. *Journal of proteome research, 5*(4), 916-924. https://doi.org/10.1021/pr0504079

Khan, M. M., Ansari, S. A., Lee, J. H., Ansari, M. O., Lee, J., & Cho, M. H. (2014). Electrochemically active biofilm assisted synthesis of Ag@ CeO2 nanocomposites for antimicrobial activity, photocatalysis and photoelectrodes. *Journal of colloid and interface science, 431*, 255-263. https://doi.org/10.1016/j.jcis.2014.06.026

Maslakov, K. I., Teterin, Y. A., Popel, A. J., Teterin, A. Y., Ivanov, K. E., Kalmykov, S. N., ... & Farnan, I. (2018). XPS study of ion irradiated and unirradiated CeO2 bulk and thin film samples. *Applied Surface Science, 448*, 154-162. https://doi.org/10.1016/j.apsusc.2018.04.077

Mokomane M., Kasvosve, I., Melo, E., Pernica, J. M., & Goldfarb, D.M. (2018). The global problem of childhood diarrhoeal diseases: emerging strategies in prevention and management. *Therapeutic Advances in Infectious Disease, 5*(1), 29-43. https://doi.org/10.1177/2049936117744429

Naika, H. R., Lingaraju, K., Manjunath, K., Kumar, D., Nagaraju, G., Suresh, D., & Nagabhushana, H. (2015). Green synthesis of CuO nanoparticles using Gloriosa superba L. extract and their antibacterial activity. *Journal of Taibah University for Science, 9*(1), 7-12. https://doi.org/10.1016/j.jtusci.2014.04.006

Park, H. J., Kim, J. Y., Kim, J., Lee, J. H., Hahn, J. S., Gu, M. B., & Yoon, J. (2009). Silver-ion-mediated reactive oxygen species generation affecting bactericidal activity. *Water research, 43*(4), 1027-1032. https://doi.org/10.1016/j.watres.2008.12.002

Pereira, A., Blouin, M., Pillonnet, A., & Guay, D. (2014). Structure and valence properties of ceria thin films synthesized by laser ablation under H2/He atmosphere. *Materials Research Express, 1*(1), 015704. https://doi.org/10.1088/2053-1591/1/1/015704

Qidwai, A., Kumar, R., Shukla, S. K., & Dikshit, A. (2018). Advances in biogenic nanoparticles and the mechanisms of antimicrobial effects. *Indian Journal of Pharmaceutical Sciences, 80*(4), 592-603. https://doi.org/ 10.4172/pharmaceutical-sciences.1000398

Rai, M., Deshmukh, S.D., Ingle, A.P., Gupta, I.R., Galdiero, M., & Galdiero, S. (2014). Metal nanoparticles: The protective nanoshield against virus infection. *Critical Reviews in Microbiology, 1*-11 https://doi.org/10.3109/1040841X.2013.879849

Sandoval, A., Aguilar, A., Louis, C., Traverse, A., & Zanella, R. (2011). Bimetallic Au–Ag/TiO2 catalyst prepared by deposition–precipitation: High activity and stability in CO oxidation. *Journal of Catalysis, 281*(1), 40-49. https://doi.org/10.1016/j.jcat.2011.04.003

Schreurs, W. J., & Rosenberg, H. (1982). Effect of silver ions on transport and retention of phosphate by Escherichia coli. *Journal of bacteriology, 152*(1), 7-13.

Shankar, S. S., Ahmad, A., Pasricha, R., & Sastry, M. (2003). Bioreduction of chloroaurate ions by geranium leaves and its endophytic fungus yields gold nanoparticles of different shapes. *Journal of Materials Chemistry, 13*(7), 1822-1826. https://doi.org/10.1039/b303808b

Sing, K. S. W. (1985). Reporting of Physisorption Data for Gas/Solids Systems with Special Reference to the Determination of Surface Area and Porosity. *Pure and Applied Chemistry, 57*, 603-619. https://doi.org/10.1351/pac198254112201

Mendiola, D. S. S., Sánchez, U. A., Palacios, M. J. A., Wang, J. A., Chen, L., & Morales, F. J. T. (2017). Bactericidal Action of Silver Nanoparticles Dispersed in Silica Synthesized through the Sol Gel Method. *Journal of Materials Science and Engineering A, 7*(9-10), 246-257. https://doi.org/10.17265/2161-6213/2017.9-10.003

Sondi, I., & Salopek-Sondi, B. (2004). Silver nanoparticles as antimicrobial agent: a case study on E. coli as a model for Gram-negative bacteria. *Journal of colloid and interface science, 275*(1), 177-182.
https://doi.org/10.1016/j.jcis.2004.02.012

Spadaro, J. A., Berger, T. J., Barranco, S. D., Chapin, S. E., & Becker, R. O. (1974). Antibacterial effects of silver electrodes with weak direct current. *Antimicrobial agents and chemotherapy, 6*(5), 637-642.
https://doi.org/10.1128/aac.6.5.637

Troeger, C., Forouzanfar, M., Rao, P. C., Khalil, I., Brown, A., Reiner Jr, R. C., ... & Alemayohu, M. A. (2017). Estimates of global, regional, and national morbidity, mortality, and aetiologies of diarrhoeal diseases: a systematic analysis for the Global Burden of Disease Study 2015. *The Lancet Infectious Diseases, 17*(9), 909-948.
https://doi.org/10.1016/S1473-3099(17)30276-1

Van Dao, D., Nguyen, T. T., Song, H. Y., Yang, J. K., Kim, T. W., Yu, Y. T., & Lee, I. H. (2018). Ionic liquid-assisted preparation of Ag-CeO2 nanocomposites and their improved photocatalytic activity. *Materials & Design, 159*, 186-194.
https://doi.org/10.1016/j.matdes.2018.08.042

Padil, V. V. T., & Černík, M. (2013). Green synthesis of copper oxide nanoparticles using gum karaya as a biotemplate and their antibacterial application. *International journal of nanomedicine, 8*, 889.
https://doi.org/10.2147/IJN.S40599

Wang, G., Ma, X., Huang, B., Cheng, H., Wang, Z., Zhan, J., ... & Dai, Y. (2012). Controlled synthesis of Ag 2 O microcrystals with facet-dependent photocatalytic activities. *Journal of Materials Chemistry, 22*(39), 21189-21194.
https://doi.org/10.1039/C2JM35010F

Wang, J. A., Aguilar-Ríos, G., & Wang, R. (1999). Inhibition of carbon monoxide on methanol oxidation over γ-alumina supported Ag, Pd and Ag–Pd catalysts. *Applied surface science, 147*(1-4), 44-51.
https://doi.org/10.1016/S0169-4332(99)00073-2

Wang, L., He, H., Yu, Y., Sun, L., Liu, S., Zhang, C., & He, L. (2014). Morphology-dependent bactericidal activities of Ag/CeO2 catalysts against Escherichia coli. *Journal of Inorganic Biochemistry, 135*, 45-53.
https://doi.org/10.1016/j.jinorgbio.2014.02.016

Warule, S. S., Chaudhari, N. S., Kale, B. B., Patil, K. R., Koinkar, P. M., More, M. A., & Murakami, R. I. (2012). Organization of cubic CeO 2 nanoparticles on the edges of self assembled tapered ZnO nanorods via a template free one-pot synthesis: significant cathodoluminescence and field emission properties. *Journal of Materials Chemistry, 22*(18), 8887-8895.
https://doi.org/10.1039/C2JM30226H

Yang, W., Shen, C., Ji, Q., An, H., Wang, J., Liu, Q., & Zhang, Z. (2009). Food storage material silver nanoparticles interfere with DNA replication fidelity and bind with DNA. *Nanotechnology, 20*(8), 085102.
https://doi.org/10.1088/0957-4484/20/8/085102